

Review

TiPd- and TiPt-Based High-Temperature Shape Memory Alloys: A Review on Recent Advances

Yoko Yamabe-Mitarai ^{1,2} 

¹ Department of Advanced Materials Science, Graduate School of Frontier Sciences, The University of Tokyo, 5-1-5 Kashiwanoha, Kashiwa-shi, Chiba 277-8561, Japan; mitarai.yoko@edu.k.u-tokyo.ac.jp

² National Institute for Materials Science, 1-2-1 Sengen, Tsukuba, Ibaraki 305-0047, Japan

Received: 30 September 2020; Accepted: 12 November 2020; Published: 18 November 2020



Abstract: In this paper high-temperature shape memory alloys based on TiPd and TiPt are reviewed. The effect of the alloying elements in ternary TiPd and TiPt alloys on phase transformation and strain recovery is also discussed. Generally, the addition of alloying elements decreases the martensitic transformation temperature and improves the strength of the martensite and austenite phases. Additionally, it also decreases irrecoverable strain, but without perfect recovery due to plastic deformation. With the aim to improve the strength of high-temperature shape memory alloys, multi-component alloys, including medium- and high-entropy alloys, have been investigated and proposed as new structural materials. Notably, it was discovered that the martensitic transformation temperature could be controlled through a combination of the constituent elements and alloys with high austenite finish temperatures above 500 °C. The irrecoverable strain decreased in the multi-component alloys compared with the ternary alloys. The repeated thermal cyclic test was effective toward obtaining perfect strain recoveries in multi-component alloys, which could be good candidates for high-temperature shape memory alloys.

Keywords: high-temperature shape memory alloys; titanium palladium; titanium platinum; multi-component alloys; medium-entropy alloys; high-entropy alloys

1. Introduction

Shape recovery in shape memory alloys (SMAs) occurs during a reverse martensitic transformation from martensite to austenite phases. Thereafter, the SMA operating temperature is related to the martensitic transformation temperature (MTT). High-temperature shape memory alloys (HT-SMAs) are defined as SMAs that can recover their shapes at temperatures above 100 °C. Several applications of HT-SMAs have been proposed. For example, Ni₃₀Pt₂₀Ti₅₀, whose MTTs include austenite start temperature, A_s : 262 °C; austenite finish temperature, A_f : 275 °C; martensite start temperature, M_s : 265 °C; and martensite finish temperature, M_f : 240 °C, was applied for active clearance control actuation in the high-pressure turbine section of a turbofan engine [1]. This indicates that the design can offer a small and lightweight package without requiring motion amplifiers that cause efficiency losses and introduce an additional failure mode [1]. Another example is the helical actuators for surge-control applications in helicopter engine compressors [2]. In this application, Ni_{19.5}Ti_{50.5}Pd₂₅Pt₅, whose MTTs comprise A_s : 243 °C, A_f : 259 °C, M_s : 247 °C, and M_f : 228 °C, was applied because the alloy exhibited good work capabilities, a 2.5% recoverable strain, and a work output of 9.45 J/cm³ at 400 MPa [2]. Several SMA applications, such as the active jet engine chevron, springs and wires for a general class of high-temperature actuators, oxygen mask deployment latch, SMA-activated thermal switch for lunar surface applications, variable geometry chevrons, and gas turbine variable area nozzles, have also been proposed [3]. Here, HT-SMAs, Ni_{19.5}Ti_{50.5}Pd₂₅Pt₅ or Ni_{50.3}Ti_{29.7}Hf₂₀ are used only in springs and

wires for a general class of high-temperature actuator. Furthermore, NiTi-based SMAs that can actuate in the temperature range of 70–90 °C are used in other applications.

Raising MTTs is necessary for the development of HT-SMAs. In addition, improving SMA strength is also important because plastic deformation easily occurs at high temperatures, thereby resulting in incomplete shape recovery. Several studies have been conducted to increase MTTs by adding alloying elements such as Hf, Zr, Pd, Pt, and Au, to NiTi [4–10]. Their MTTs successfully increased by adding an alloying element, but a perfect shape recovery was not obtained. Recently, research of NiTi alloys has shifted to Ni_{50.3}Ti_{29.7}Hf₂₀, which is strengthened by nano-size precipitates called the “H phase” [11–24]. The austenite finishing temperature A_f of Ni_{50.3}Ti_{29.7}Hf₂₀ is typically 166 °C under unloading conditions [13], but it rises to 270 °C under tensile loading conditions at 500 MPa [16]. Furthermore, ageing increased the work output due to the higher transformation strain and the work output under 500 MPa was 16.45 J/cm³ at A_f of 270 °C [16]. High strength Ni-rich Ni_{51.2}Ti_{28.8}Hf₂₀ was also developed and its work output was 23 J/cm³ under 1700 MPa at A_f of approximately 100 °C, 27 J/cm³ under 1500 MPa at A_f of approximately 220 °C, and 15 J/cm³ under 1000 MPa at A_s of 151 °C (A_f was not clearly shown) [19]. The effect of 2000 thermal training cycles under 300 MPa of Ni_{50.3}Ti_{29.7}Hf₂₀ was also investigated and it was found that the stable cyclic strain recovery with the almost constant transformation strain [24]. The work output under 300 MPa was approximately 7.5 J/cm³ at A_f of approximately 220 °C [24].

Another approach to increasing MTTs is using other alloys with MTTs higher than those of NiTi alloys. Therefore, TiPd, TiAu, and TiPt have been studied because they exhibit a martensitic transformation from a B2 to a B19 structure, and their MTT values are higher than 500 °C [25,26]. For example, typical martensitic twin structures were observed in TiPt, whose high potential as an HT-SMA has been established [27,28]. The first investigation on strain recovery at high temperatures was performed for TiPd [29]. A binary TiPd sample was deformed at 500 °C, and the change in its length after it was heated above the A_f was investigated to measure strain recovery [29]. However, only a 10% strain was recovered owing to plastic deformation at 500 °C [29]. The shape recovery behavior of the TiAu alloy was investigated through thermomechanical analysis measurements after compressive deformation at 500 °C [30]. It was found that an 80% strain recovery occurred after a 5% deformation [30]. The effects of both Zr [31] and Ag addition [32] into TiAu on the martensitic transformation and strain recovery was investigated; the MTT decreased by 10% with the addition of Zr and Ag. For example, A_f decreased from 624 °C for TiAu to 511 °C and 594 °C for Ti–50Au–10Zr and Ti–40Au–10Ag, respectively [31,32]. Compressive deformation was applied at a test temperature of 50 °C below M_f , and the deformed samples were heated above A_f to measure the strain recovery. The strain recovery ratios of the Ti–50Au, Ti–50Au–10Zr, and Ti–40Au–10Ag alloys were 68%, 82%, and 76%, respectively [32]. The addition of Zr and Ag was effective in improving the strain recovery of TiAu.

The effects of an alloying element on MTTs, strain recovery, as well as strength of the martensite and austenite phases in TiPd and TiPt alloys, have been investigated by my group [33–50] and are reviewed herein. In addition to the TiPd and TiPt alloys, high- and medium- entropy SMAs (HEAs or MEAs) are also appraised because HEAs and MEAs have been attracting considerable attention as new SMAs. Notably, HEAs and MEAs are multi-component equiatomic or near-equiatomic alloys, which have garnered much interest as new generation structural materials because their high-entropy effects, such as severe lattice distortion and sluggish diffusion, are expected to improve the high-temperature strength of alloys [51,52]. As already shown, it is difficult to achieve perfect strain recovery in HT-SMAs because of the easy introduction of plastic deformation at high temperatures. Furthermore, improvement of strength of SMAs is a key issue for HT-SMAs. Application of HEAs and MEAs to HT-SMAs is expected in this area for which results on multi-component alloys, in particularly MEAs and HEAs, are presented in this paper.

2. Martensitic Transformation Temperature

The MTTs of the TiPd and TiPt alloys measured through differential scanning calorimetry (DSC) (DSC3200, NETZSCH Japan, Yokohama, Japan) are shown in Table 1. The temperature hysteresis, A_f-M_s , is also summarized in Table 1. Data without reference are from my group's unpublished work. The addition of a third element, such as Hf, Zr, V, Nb, Ta, Cr, Mo, W, Ru, Ir, and Co, was performed for TiPd, while elements, including Ir, Ru, Co, Zr, and Hf, were added for TiPt. In most cases, the MTT decreased with the addition of an alloying element. In Figure 1a, A_f changes with increasing alloying element concentration are shown for some of the ternary alloys. Notably, A_f decreased rather linearly with increasing amounts of alloying elements. The same trend appeared for A_s , M_s , and M_f . The average decrease in M_s per 1 at% of an alloying element up to 5 at% addition is shown in Table 1. Ta and W did not melt well into TiPd, and their particles remained in the alloy, thereby making the matrix composition of $Ti_{45}Pd_{50}W_5$ and $Ti_{45}Pd_{50}Ta_5$ approximately close to that of TiPd. Consequently, the decrease in the MTT by W and Ta was small. For other alloying elements, the decrease in MTT was between 15–37 °C. In Figure 1b, the MTT change with respect to Pd concentration is observed for $Ti_{(95-x)}Pd_xZr_5$; the MTT increased with an increase in the Pd concentration.

Table 1. Martensitic transformation temperature of ternary alloys (°C).

Alloy	Austenite Start Temperature A_s	Austenite Finish Temperature A_f	Martensite Start Temperature M_s	Martensite Finish Temperature M_f	Temperature Hysteresis A_f-M_s	Average Decrease in M_s per 1 at% $\Delta M_s/at\%$	Ref.
Ti ₅₀ Pd ₅₀	568	587	527	515	60	-	[33]
Ti ₄₈ Pd ₅₀ Hf ₂	538	570	494	472	76	-	
Ti ₄₅ Pd ₅₀ Hf ₅	481	505	460	429	45	-15	[34]
Ti ₄₀ Pd ₅₀ Hf ₁₀	227	306	276	188	30	-	
Ti ₄₀ Pd ₅₅ Hf ₅	528	551	471	487	80	-	[35]
Ti ₄₇ Pd ₅₀ Zr ₃	520	533	491	470	42	-	
Ti ₄₅ Pd ₅₀ Zr ₅	492	508	467	445	41	-15	[33]
Ti ₄₃ Pd ₅₀ Zr ₇	491	506	464	443	42	-	[36]
Ti ₄₀ Pd ₅₀ Zr ₁₀	256	308	221	204	87	-	[33,36]
Ti ₅₀ Pd ₄₅ Zr ₅	324	374	344	312	30	-	
Ti ₄₇ Pd ₄₈ Zr ₅	429	450	370	331	80	-	
Ti ₄₃ Pd ₅₂ Zr ₅	482	529	393	366	136	-	
Ti ₄₀ Pd ₅₅ Zr ₅	530	593	451	438	142	-	[35]
Ti ₄₅ Pd ₅₀ V ₅	508	523	462	440	61	-15	[34]
Ti ₄₀ Pd ₅₅ V ₅	437	559	442	398	117	-	[35]
Ti ₄₅ Pd ₅₀ Nb ₅	486	508	431	408	77	-20	[34]
Ti ₄₀ Pd ₅₅ Nb ₅	487	535	409	360	126	-	[35]
Ti ₄₅ Pd ₅₀ Ta ₅ *	561	579	512	489	67	-4	[34]
Ti ₄₅ Pd ₅₀ Cr ₅	268	356	347	293	9	-37	[34]
Ti ₄₅ Pd ₅₀ Mo ₅	267	383	401	268	-18	-27	[34]
Ti ₄₅ Pd ₅₀ W ₅ *	558	576	513	492	63	-4	[34]
Ti ₅₀ Pd ₄₈ Ru ₂	561	576	516	510	60	-	[37]
Ti ₅₀ Pd ₄₆ Ru ₄	440	482	436	393	46	-23	[37]
Ti ₅₀ Pd ₄₂ Ru ₈	298	354	333	275	22	-	[37]
Ti ₅₀ Pd _{37.5} Ru _{12.5}	-	-	-	-	-	-	[37]
Ti ₅₀ Pd ₂₅ Ru ₂₅	-	-	-	-	-	-	[37]
Ti ₅₀ Pd ₄₈ Ir ₂	556	581	508	500	73	-	[37]
Ti ₅₀ Pd ₄₆ Ir ₄	525	552	510	484	42	-4	[37]
Ti ₅₀ Pd ₄₂ Ir ₈	478	521	479	439	43	-	[37]
Ti ₅₀ Pd ₃₈ Ir ₁₂	471	508	452	395	56	-	
Ti ₅₀ Pd _{37.5} Ir _{12.5}	478	492	452	433	39	-	[37]
Ti ₅₀ Pd ₂₅ Ir ₂₅	-	-	-	-	-	-	[37]
Ti ₅₀ Pd _{12.5} Ir _{37.5}	-	-	-	-	-	-	[37]
Ti ₅₀ Pd ₄₈ Co ₂	523	545	478	464	67	-	[37]
Ti ₅₀ Pd ₄₆ Co ₄	473	493	455	427	38	-18	[37]
Ti ₅₀ Pd ₄₂ Co ₈	375	398	259	327	34	-	[37]
Ti ₅₀ Pt ₅₀	1000	1057	989	963	68	-	[38]

Table 1. Cont.

Alloy	Austenite Start Temperature A_s	Austenite Finish Temperature A_f	Martensite Start Temperature M_s	Martensite Finish Temperature M_f	Temperature Hysteresis A_f-M_s	Average Decrease in M_s per 1 at% $\Delta M_s/\text{at}\%$	Ref.
Ti ₅₀ Pt ₄₅ Ir ₅	1050	1081	1030	1008	51	-	[39,40]
Ti ₅₀ Pt _{37.5} Ir _{12.5}	1036	1103	1000	978	103	-	[38]
Ti ₅₀ Pt ₂₅ Ir ₂₅	1121	1190	1110	1068	80	-	[38]
Ti ₅₀ Pt ₂₀ Ir ₃₀	1159	1189	1145	1127	44	-	[39]
Ti ₅₀ Pt _{12.5} Ir _{37.5}	1175	1218	1184	1169	34	-	[38]
Ti ₅₅ Pt ₃₅ Ir ₁₀	931	959	-	-	-	-	[41]
Ti ₅₀ Pt ₄₅ Ru ₅	925	975	913	856	62	-20	[40,42]
Ti ₄₅ Pt ₅₀ Zr ₅	939	985	897	840	88	-23	[40,42]
Ti ₅₀ Pt ₄₅ Co ₅	959	1003	913	855	90	-15	[40,43]
Ti ₄₅ Pt ₅₀ Hf ₅	952	996	905	855	91	-17	[40,44]

*: melting was not perfect.

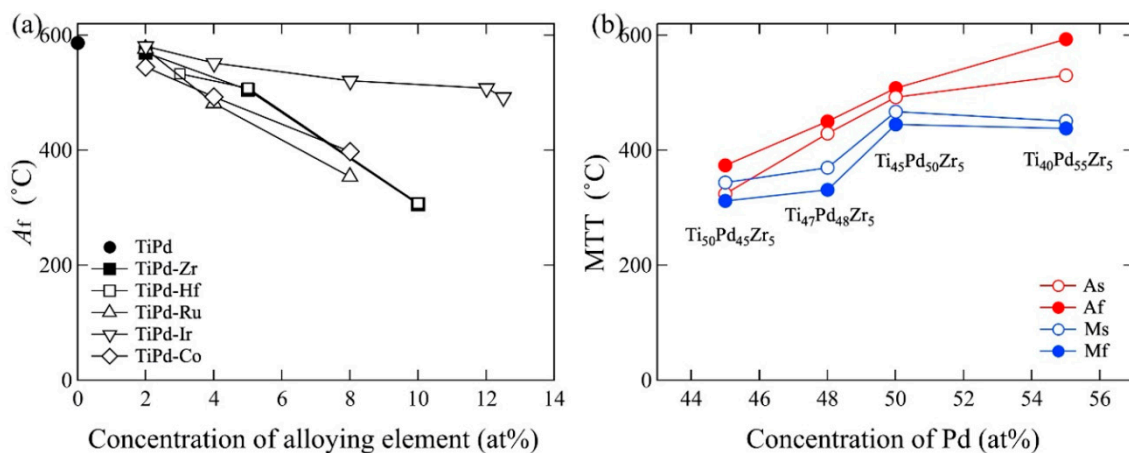


Figure 1. (a) Austenite finish temperature change for concentration of alloying element of TiPd [33], TiPd-Zr [33,36], TiPd-Hf [34], TiPd-Ru [37], TiPd-Ir [37], and TiPd-Co [37], and (b) martensite transformation temperature for concentration of Pd of Ti₅₀Pd₄₅Zr₅, Ti₄₇Pd₄₈Zr₅, Ti₄₅Pd₅₀Zr₅ [33], and Ti₄₀Pd₅₅Zr₅ [35].

The MTT of TiPt was very high; for example, A_s and A_f were 1000 °C and 1057 °C, respectively, as shown in Table 1. Although the addition of Ru, Co, Zr, and Hf decreased the MTT of TiPt, the addition of Ir increased it.

The MTTs of multi-component alloys are summarized in Table 2. Data without reference are from my group's unpublished work. The multi-component alloys were designed based on TiPd as follows: Pd, a group 10 element in the periodic table, was replaced by Co and Ir, which are group 9 elements; by Ni and Pt which are group 10 elements; and by Au, a group 11 element. Furthermore, Ti, a group 4 element, was replaced by Zr and Hf, which are also group 4 elements. Evident DSC peaks were not observed in the three alloys, Ti₄₀Zr₁₀Pd₂₅Pt₂₅, Ti₄₅Zr₅Pd₃₇Ni₁₃, and Ti₄₅Zr₅Pd₂₅Pt₂₀Ni₅, and their MTTs were estimated from the strain–temperature (S – T) curves during the thermal cyclic test under constant stress.

Table 2. Martensitic transformation temperature of multi-element alloys.

Alloy	A_s	A_f	M_s	M_f	$A_f - M_s$	ΔS_{mix}	Alloy Classification	Ref.
Ti ₄₅ Zr ₅ Pd ₄₅ Ir ₅	457	475	422	398	53	1.0R	Low-entropy alloy LEA	-
Ti ₄₅ Zr ₅ Pd ₃₅ Ir ₁₅	313	348	295	256	53	1.2R	Medium-entropy alloy MEA	-
Ti ₄₅ Zr ₅ Pd ₂₅ Ir ₂₅	-	-	-	-	-	1.2R	MEA	-
Ti ₄₅ Zr ₅ Pd ₄₅ Pt ₅	497	511	464	439	47	1.0R	LEA	[45]
Ti ₄₅ Zr ₅ Pd ₃₅ Pt ₁₅	539	557	485	471	72	1.2R	MEA	[45]
Ti ₄₅ Zr ₅ Pd ₂₅ Pt ₂₅	628	648	571	539	77	1.2R	MEA	[45]
Ti ₄₅ Zr ₅ Pd ₁₅ Pt ₃₅	725	804	713	590	91	1.2R	MEA	[46]
Ti ₄₅ Zr ₅ Pd ₅ Pt ₄₅	896	935	774	713	112	1.0R	LEA	[46]
Ti ₄₀ Zr ₁₀ Pd ₂₅ Pt ₂₅	390	430	245	220	288	1.3R	MEA	[47] ST
Ti ₄₅ Zr ₄ V ₁ Pd ₅₀	497	508	409	384	99	0.9R	LEA	[36]
Ti ₄₅ Zr _{2.5} V _{2.5} Pd ₅₀	523	546	393	368	153	0.9R	LEA	[36]
Ti ₄₅ Zr ₁ V ₄ Pd ₅₀	496	518	441	424	77	0.9R	LEA	[36]
Ti ₄₅ Zr ₅ Pd ₄₅ Ni ₅	348	378	328	297	50	1.0R	LEA	[47]
Ti ₄₅ Zr ₅ Pd ₄₀ Ni ₁₀	216	258	206	177	52	1.1R	MEA	[48]
Ti ₄₅ Zr ₅ Pd ₃₇ Ni ₁₃	114	230	206	108	24	1.2R	MEA	[47] ST
Ti ₄₂ Zr ₈ Pd ₄₀ Ni ₁₀	-	-	-	-	-	1.2R	MEA	[47]
Ti ₄₅ Zr ₅ Pd ₃₀ Ni ₂₀	-	-	-	-	-	1.2R	MEA	[48]
Ti ₄₅ Zr ₅ Pd ₄₀ Co ₁₀	303	361	339	298	22	1.1R	MEA	[48]
Ti ₄₅ Zr ₅ Pd ₄₀ Ni ₈ Co ₂	201	273	212	199	61	1.2R	MEA	[48]
Ti ₄₅ Zr ₅ Pd ₄₀ Ni ₅ Co ₅	-	-	-	-	-	1.2R	MEA	[48]
Ti ₄₅ Zr ₅ Pd ₄₀ Ni ₂ Co ₈	143	189	135	108	54	1.2R	MEA	[48]
Ti ₃₅ Zr ₁₅ Pd ₂₀ Pt ₁₅ Ni ₁₅	-	-	-	-	-	1.5R	High-entropy alloy HEA	[49]
Ti ₄₀ Zr ₁₀ Pd ₂₀ Pt ₁₅ Ni ₁₅	-	-	-	-	-	1.5R	HEA	[49]
Ti ₄₅ Zr ₅ Pd ₂₀ Pt ₂₅ Ni ₅	559	598	502	432	96	1.3R	MEA	[49]
Ti ₄₅ Zr ₅ Pd ₂₅ Pt ₂₀ Ni ₅	390	430	245	220	185	1.3R	MEA	[47] ST
Ti ₄₅ Zr ₅ Pd ₂₀ Pt ₂₀ Ni ₁₀	374	442	337	256	105	1.3R	MEA	[49]
Ti ₃₅ Zr ₁₅ Pd ₂₀ Pt ₁₅ Au ₁₅	-	-	-	-	-	1.5R	HEA	[50]
Ti ₃₅ Zr ₁₅ Pd ₂₀ Pt ₁₅ Co ₁₅	-	-	-	-	-	1.5R	HEA	[50]
Ti ₄₅ Zr ₅ Pd ₂₅ Pt ₂₀ Au ₅	520	590	515	453	75	1.3R	MEA	[50]
Ti ₄₅ Zr ₅ Pd ₂₅ Pt ₂₀ Co ₅	419	538	431	324	107	1.3R	MEA	[50]
Ti _{16.7} Zr _{16.7} Hf _{16.7} Ni ₂₅ Cu ₂₅	184	338	226	112	112	1.6R	HEA	[53]
Ti _{16.7} Zr _{16.7} Hf _{16.7} Ni ₂₅ Co ₁₀ Cu ₁₅	-23	71	36	-80	35	1.8R	HEA	[54]
Ti ₃₀ Hf ₂₀ Pd ₁₅ Ni ₃₅	537	686	525	479	161	1.3R	MEA	[55]
Ti ₂₅ Hf ₂₅ Pd ₂₅ Ni ₂₅	680	720	620	580	100	1.4R	MEA	[55]
Ti _{16.7} Zr _{16.7} Hf _{16.7} Pd ₂₅ Ni ₂₅	740	780	660	620	120	1.6R	HEA	[55]

Multi-component alloys are classified according to the mixing entropy, ΔS_{mix} , using the following equations [51].

Here, ΔS_{mix} is defined by the following equation:

$$\Delta S_{mix} = -R \sum_{i=1}^n x_i \ln x_i \quad (1)$$

where x_i is the mole fraction of component i , n is the number of constituent elements, and R is the gas constant (8.314 J/Kmol).

HEA:

$$\Delta S_{mix} \geq 1.5R \quad (2)$$

Medium-entropy alloy (MEA):

$$1.0R \leq \Delta S_{mix} \leq 1.5R \quad (3)$$

Low-entropy alloy (LEA, conventional solid-solution alloy):

$$\Delta S_{\text{mix}} \leq 1.0R \quad (4)$$

The calculated mixing entropies are presented in Table 2. Based on the mixing entropies, the alloy classification is also shown in Table 2. Most quaternary alloys are classified as MEAs, while some are classified as LEAs, i.e., conventional solid-solution alloys. Notably, HEAs have been identified in some multi-component alloys with five or six constituent elements.

The MTTs of the five quaternary alloys, TiZrPdIr, TiZrPdPt, TiZrPdNi, TiZrPdCo, and TiZrVPd, are shown in Table 2. The combination of TiZrPdIr, TiZrPdNi, and TiZrPdCo decreased the MTTs compared with those of Ti₄₅Zr₅Pd₅₀. This is because the phase transformations of TiIr, TiNi, and TiCo are different from those of TiPd. For example, TiIr undergoes a two-step phase transformation from the B2 structure at high temperature to a tetragonal structure (distorted B2 structure) at middle temperature, and finally to an orthorhombic structure with space group 65 at low temperature [56]. The MTT depends on Ir concentration. Notably, TiNi undergoes martensitic transformation from the B2 to the B19' structure [4]. The B2 structure is very stable in TiCo from room temperature to the melting temperature [25]; the addition of these elements is considered to stabilize the B2 structure. However, TiZrPdPt increased the MTT relative to Ti₄₅Zr₅Pd₅₀. This is because the same martensitic transformation from B2 to B19 structures, as well as TiPd, occur in TiPt, whose MTT is very high, approximately 1000 °C, as shown in Table 1. Furthermore, Pt and Pd exhibit perfect solubility in both austenite and martensite phases. Consequently, MTT gradually increased with Pt content. In the case of TiZrVPd, the total amounts of Zr and V were maintained at 5 at%, and the values of A_s and A_f were approximately the same as those of Ti₄₅Zr₅Pd₅₀, while the M_s and M_f values of TiZrVPd were lower than those of Ti₄₅Zr₅Pd₅₀.

Although the MTTs of multi-component alloys depend on the combination of elements, there are some trends whereby those of TiZrPdPtNi and TiZrPdPtAu are relatively high, whereas that of TiZrPdNiCo is relatively low.

The potential of HEAs as SMAs was presented for the first time by Fistov et al., wherein Ti_{16.7}Zr_{16.7}Hf_{16.7}Ni₂₅Cu₂₅ was investigated and its A_s and A_f were 184 and 338 °C, respectively [53]. The addition of Co to Ti_{16.7}Zr_{16.7}Hf_{16.7}Ni₂₅Cu₂₅ was investigated, but its MTT drastically decreased and A_f was −23 °C [54]. The MTTs of these alloys are summarized in Table 2. The potential of HEAs as HT-SMAs was first shown by Canadinc [55]. The MTT of their alloys was obtained from the DSC curves in reference [55] and is summarized in Table 2. The A_s and A_f of Ti_{16.7}Zr_{16.7}Hf_{16.7}Pd₂₅Ni₂₅ were 740 and 780 °C, respectively. In my group's experiments, HEAs and some MEAs did not show martensitic transformation up to 700 °C during DSC measurement. However, martensitic transformation may be possible for these alloys at temperatures higher than 700 °C. The MTT measurement of my group's HEAs is presently undergoing ultra-high temperature DSC. We found that some alloys have a high MTT, approximately close to 1000 °C in multi-component alloys.

Notably, the temperature hysteresis of the multi-component alloys becomes larger relative to that of ternary alloys. The number of alloys with temperature hysteresis exceeding 100 °C and their ratios are summarized in Table 3. The ratio of alloys with temperature hysteresis exceeding 100 °C in ternary alloys is 12% and it increases to 28% in LEAs and to 40% in MEAs and HEAs. It indicates that the ratio of alloys with temperature hysteresis exceeding 100 °C increased with increase of amount of constituent elements in alloys. In multi-component alloys, in particularly in MEAs and HEAs, the amount of constituent elements is equivalent or near-equivalent; therefore, it is expected that severe lattice distortion, which is considered to obstruct martensitic transformation, will occur. In many MEA cases, a drastic decrease in M_s was observed compared with A_f . When SMAs are used as actuators, a smaller temperature hysteresis is necessary to quickly respond to the surrounding environment.

Table 3. Ratio of alloys with temperature hysteresis over 100 °C (%).

Alloys	Number of Alloys with Temperature Hysteresis over 100 °C	Number of Tested Alloys	Ratio of Alloys with Temperature Hysteresis over 100 °C (%)
Ternary alloy in Table 1	5	42	12
LEA in Table 2	2	7	28
MEA and HEA in Table 2	8	20	40

3. Strain Recovery Determined by Compression Test

In the early stage of my group's research [33–35,37–44], the recovery strain was estimated by measuring the sample length before and after the compression test using a strain rate of 3×10^{-3} /s, and after heat treatment above A_f . A sample was deformed by approximately 5% at the test temperature. The deformed sample length (L') was measured after cooling to room temperature. Thereafter, the sample was re-heated over A_f , cooled to room temperature, and the recovered sample length (L'') was measured. When the initial sample length is L_0 , the applied strain ϵ_a is defined by the following equation:

$$\epsilon_a = 100 \times ((L_0 - L')/L_0) \quad (5)$$

Recoverable strain ϵ_r is defined according to the following equation:

$$\epsilon_r = 100 \times ((L'' - L')/L_0) \quad (6)$$

Strain recovery ratio, i.e., shape memory effect (SME) was evaluated using the following equation:

$$\text{SME (\%)} = \epsilon_r/\epsilon_a \times 100 \quad (7)$$

The applied and recoverable strains, as well as the strain recovery ratios of the ternary TiPd and TiPt alloys, are summarized in Table 4. Data without reference are from my group's unpublished work. For the quaternary alloys, this method was used only for TiZrPdIr, and the results are summarized in Table 5. Although it is difficult to compare the effect of alloying elements due to different applied strains, some alloys have a high strain recovery ratio of above 80%. The quaternary alloys also exhibited a high strain recovery ratio of above 80%, as shown in Table 5. In Figure 2, the strain recovery ratios of $\text{Ti}_{45}\text{Pd}_{50 \times 5}$ are plotted for the periodic table family; it can be observed that the addition of Zr and Hf is effective toward improving strain recovery. Since the atomic size (metallic) of Zr and Hf are 160 and 159 pm, respectively, and larger than those of Ti (147 pm) and Pd (137 pm) [57], the solid-solution hardening effects of Zr and Hf are considered to exceed those of the other alloying elements. Thereafter, the 0.2% flow stress of the austenite and martensite phases were investigated by compression testing using samples with dimensions of $2.5 \times 2.5 \times 5 \text{ mm}^3$. The 0.2% flow stresses of ternary TiPd and TiPt alloys are summarized in Table 6. Data without reference are from my group's unpublished work. When the martensite phase is deformed, a double yielding behavior often occurs. The first yielding behavior represents the rearrangement of the martensite variant and is referred to as the detwinning stress. The second yielding behavior represents the yield stress of martensite. In Table 6, the detwinning stresses of the martensite phase are also shown. In Figure 3, the 0.2% flow stress of the austenite and martensite phases of $\text{Ti}_{45}\text{Pd}_{50}\text{X}_5$ (X in group 4–6 elements) and $\text{Ti}_{50}\text{Pd}_{46}\text{Y}_4$ (Y in group 8–10 elements) are plotted for the periodic table family. Most alloying elements improved the strength of the austenite and martensite phases compared with those of $\text{Ti}_{50}\text{Pd}_{50}$. The strengthening behavior of the alloying element on the austenite and martensite phases was similar. Comparing Figures 2 and 3, it is evident that high-strength alloys, such as $\text{Ti}_{45}\text{Pd}_{50}\text{V}_5$, have a lower strain recovery than $\text{Ti}_{45}\text{Pd}_{50}\text{Zr}_5$ and $\text{Ti}_{45}\text{Pd}_{50}\text{Hf}_5$ with a smaller strengthening effect than $\text{Ti}_{45}\text{Pd}_{50}\text{V}_5$. It is difficult to establish the correlation between strength and strain recovery ratio.

Table 4. Strain recovery of ternary alloys.

Alloy	Test Temp., °C	The Difference from Martensite Transformation Temperature, °C	Applied Strain, %	Recoverable Strain, %	Strain Recovery Ratio, %	Ref.
Ti ₅₀ Pd ₅₀	538	-	4.1	1.6	40	[33]
Ti ₅₀ Pd ₅₀	485	$M_f - 30$	3.8	2.5	67	[34]
Ti ₅₀ Pd ₅₀	380	-	3.7	0.46	13	[33]
Ti ₅₀ Pd ₅₀	320	-	1.24	0.59	48	
Ti ₄₈ Pd ₅₀ Hf ₂	380	-	2.8	0.4	14	
Ti ₄₅ Pd ₅₀ Hf ₅	456	$A_s - 30$	2.9	2.1	74	
Ti ₄₅ Pd ₅₀ Hf ₅	440	-	2.7	2.3	80	[34]
Ti ₄₅ Pd ₅₀ Hf ₅	380	$M_f - 50$	1.9	1.5	80	
Ti ₄₅ Pd ₅₀ Hf ₅	200	-	5.25	4.1	78	
Ti ₄₀ Pd ₅₀ Hf ₁₀	380	-	3.0	2.4	80	
Ti ₄₀ Pd ₅₅ Hf ₅	457	$M_f - 30$	3.7	1.7	45	[35]
Ti ₅₀ Pd ₄₅ Zr ₅	210	-	4.28	0.7	17	
Ti ₅₀ Pd ₄₅ Zr ₅	295	-	3.1	0.55	18	
Ti ₅₀ Pd ₄₅ Zr ₅	380	-	3.2	1.47	46	
Ti ₄₇ Pd ₄₈ Zr ₅	301	-	4.2	3.6	85	
Ti ₄₇ Pd ₄₈ Zr ₅	399	-	8.3	5.7	69	
Ti ₄₇ Pd ₄₈ Zr ₅	380	-	2.2	1.1	50	
Ti ₄₈ Pd ₅₀ Zr ₂	400	-	6.5	3.4	53	
Ti ₄₈ Pd ₅₀ Zr ₂	380	-	3.1	1.3	43	
Ti ₄₇ Pd ₅₀ Zr ₃	490	$A_s - 30$	3.7	2.6	70	
Ti ₄₇ Pd ₅₀ Zr ₃	415	$M_f - 30$	3.3	2.9	88	
Ti ₄₇ Pd ₅₀ Zr ₃	380	-	3.2	2.8	87	
Ti ₄₅ Pd ₅₀ Zr ₅	415	$M_f - 30$	4.4	3.5	81	[34]
Ti ₄₅ Pd ₅₀ Zr ₅	426	$A_s - 30$	3.1	2.58	84	[33]
Ti ₄₅ Pd ₅₀ Zr ₅	460	-	8	5.2	65	
Ti ₄₅ Pd ₅₀ Zr ₅	380	-	3.5	2.2	62	
Ti ₄₅ Pd ₅₀ Zr ₅	380	-	4.1	3.9	94	[33]
Ti ₄₃ Pd ₅₂ Zr ₅	380	-	2.2	1.75	81	
Ti ₄₃ Pd ₅₂ Zr ₅	451	$A_s - 30$	4.6	4.1	90	
Ti ₄₀ Pd ₅₅ Zr ₅	490	-	7.2	2.0	27	
Ti ₄₀ Pd ₅₅ Zr ₅	450	-	1.2	0.39	34	

Table 4. Cont.

Alloy	Test Temp., °C	The Difference from Martensite Transformation Temperature, °C	Applied Strain, %	Recoverable Strain, %	Strain Recovery Ratio, %	Ref.
Ti ₄₀ Pd ₅₅ Zr ₅	380	-	1.9	0.4	22	
Ti ₄₃ Pd ₅₀ Zr ₇	461	$A_s - 30$	1.4	1.2	84	
Ti ₄₃ Pd ₅₀ Zr ₇	413	$M_f - 30$	3.6	3.6	100	
Ti ₄₃ Pd ₅₀ Zr ₇	380	-	3.2	2.9	90	
Ti ₄₀ Pd ₅₀ Zr ₁₀	225	-	7.7	4.8	63	[33]
Ti ₄₀ Pd ₅₀ Zr ₁₀	380	-	1.4	1.4	100	
Ti ₄₀ Pd ₅₅ Zr ₅	408	$M_f - 30$	4	1.2	30	[35]
Ti ₄₅ Pd ₅₀ V ₅	413	$M_f - 30$	2.4	1.2	60	[34]
Ti ₄₀ Pd ₅₅ V ₅	368	$M_f - 30$	3	0.3	10	[35]
Ti ₄₅ Pd ₅₀ Nb ₅	378	$M_f - 30$	3.1	1.1	37	[34]
Ti ₄₀ Pd ₅₅ Nb ₅	330	$M_f - 30$	3	0.3	10	[35]
Ti ₄₅ Pd ₅₀ Ta ₅ *	483	$M_f - 30$	3.0	1.1	35	[34]
Ti ₄₅ Pd ₅₀ Cr ₅	228	$M_f - 30$	3.3	0.4	12	[34]
Ti ₄₅ Pd ₅₀ Mo ₅	256	$M_f - 30$	2.8	0.4	14	[34]
Ti ₄₅ Pd ₅₀ W ₅ *	474	$M_f - 30$	2.3	0.5	22	[34]
Ti ₅₀ Pd ₄₆ Ru ₂	320	-	-	-	40	[37]
Ti ₅₀ Pd ₄₆ Ru ₄	320	-	3.7	2.0	52	
Ti ₅₀ Pd ₄₂ Ru ₈	320	-	3.4	2.5	72	
Ti ₅₀ Pd ₄₈ Ir ₂	320	-	2.6	1.22	47	[37]
Ti ₅₀ Pd ₄₆ Ir ₄	320	-	2.9	1.49	51	[37]
Ti ₅₀ Pd ₄₆ Ir ₄	454	$M_f - 30$	1.0	1.0	100	
Ti ₅₀ Pd ₄₆ Ir ₄	427	$M_f - 60$	2.9	0.55	19	
Ti ₅₀ Pd ₄₂ Ir ₈	320	-	2.17	1.25	57	[37]
Ti ₅₀ Pd ₄₂ Ir ₈	408	$M_f - 30$	1.5	1.3	87	
Ti ₅₀ Pd ₄₂ Ir ₈	427	$M_f - 60$	6.36	2.05	32	
Ti ₅₀ Pd ₃₈ Ir ₁₂	401	$M_f - 30$	1.4	1.01	72	
Ti ₅₀ Pd ₄₈ Co ₂	320	-	2.35	1.36	58	[37]
Ti ₅₀ Pd ₄₆ Co ₄	320	-	3.2	1.4	47	[37]
Ti ₅₀ Pd ₄₂ Co ₈	320	-	3.3	1.0	31	[37]
Ti ₅₀ Pt ₅₀	910	$M_f - 50$	6	0	0	[38]
Ti ₅₀ Pt ₅₀	850	-	-	-	11	[39]
Ti ₅₀ Pt ₄₅ Ir ₅	850	-	-	-	10	[39,40]
Ti ₅₀ Pt _{37.5} Ir _{12.5}	928	$M_f - 50$	17	2	12	[38]
Ti ₅₀ Pt _{37.5} Ir _{12.5}	850	-	-	-	51	[39]
Ti ₅₀ Pt ₂₅ Ir ₂₅	1018	$M_f - 50$	17	4	23	[38]

Table 4. Cont.

Alloy	Test Temp., °C	The Difference from Martensite Transformation Temperature, °C	Applied Strain, %	Recoverable Strain, %	Strain Recovery Ratio, %	Ref.
Ti ₅₀ Pt ₂₅ Ir ₂₅	850	-	-	-	57	[39]
Ti ₅₀ Pt ₂₀ Ir ₃₀	850	-	-	-	36	[39]
Ti ₅₀ Pt _{12.5} Ir _{37.5}	1119	$M_f - 50$	15	0	0	[38]
Ti ₅₀ Pt _{12.5} Ir _{37.5}	850	-	-	-	21	[39]
Ti ₅₅ Pt ₃₅ Ir ₁₀	850	-	4.8	1	20	[41]
Ti ₅₆ Pt ₂₂ Ir ₂₂	850	-	2.5	1.4	56	[41]
Ti ₅₈ Pt ₁₀ Ir ₃₂	850	-	1.9	1.4	73	[41]
Ti ₅₀ Pt ₄₅ Ru ₅	802	$M_f - 50$	2.9	1.3	45	[40,42]
Ti ₄₅ Pt ₅₀ Zr ₅	790	$M_f - 50$	2.1	1.2	58	[40,42]
Ti ₅₀ Pt ₄₅ Co ₅	801	$M_f - 50$	2.5	0.9	36	[40,43]
Ti ₄₅ Pt ₅₀ Hf ₅	806	$M_f - 50$	2.4	1.4	58	[40,44]

*: melting was not perfect.

Table 5. Strain recovery of quaternary alloys.

Alloy	Test Temp., °C	The Difference from Martensite Transformation Temperature, °C	Applied Strain, %	Recoverable Strain, %	Strain Recovery Ratio, %
Ti ₄₅ Pd ₄₅ Ir ₅ Zr ₅	368	$M_f - 30$	2.8	2.7	96
Ti ₄₅ Pd ₃₅ Ir ₁₅ Zr ₅	226	$M_f - 30$	2.6	2.2	85

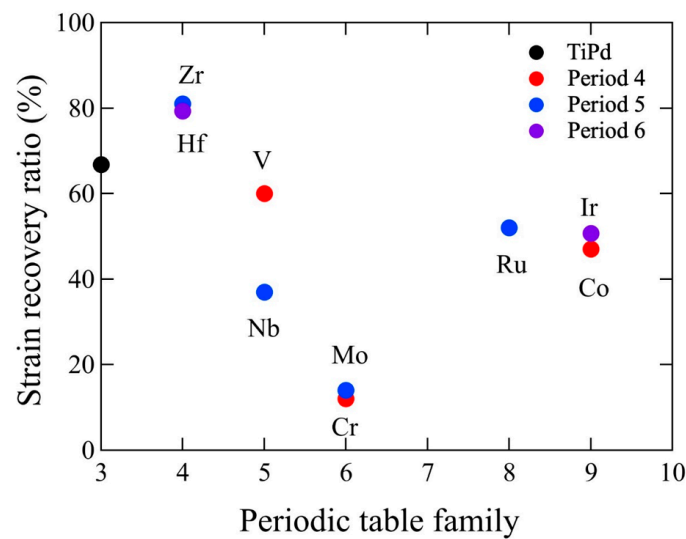


Figure 2. Strain recovery ratio of TiPd [33], $Ti_{45}Pd_{50}X_5$ ($X = Zr$ [33], Hf [34], V [34], Nb [34], Cr [34], and Mo [34]) and $Ti_{50}Pd_{46}Y_4$ ($Y = Ru, Co, \text{ and } Ir$) [37] for the periodic table family.

Table 6. Strength of the martensite and austenite phases of the binary and ternary alloys.

Alloy	Test Temp., °C	The Difference from Martensite Transformation Temperature, °C	Detwining Stress, MPa	0.2% Flow Stress, MPa	Ref.
$Ti_{50}Pd_{50}$	617	$A_f + 30$	-	82	[33]
$Ti_{50}Pd_{50}$	538	$A_s - 30$	231	293	[33]
$Ti_{50}Pd_{50}$	485	$M_f - 30$	249	617	
$Ti_{45}Pd_{50}Hf_5$	534	$A_f + 30$	-	267	[34]
$Ti_{45}Pd_{50}Hf_5$	456	$A_s - 30$	152	794	[34]
$Ti_{40}Pd_{55}Hf_5$	581	$A_f + 30$	-	341	[35]
$Ti_{40}Pd_{55}Hf_5$	441	$M_f - 30$	725	1300	[35]
$Ti_{47}Pd_{48}Zr_5$	301	$M_f - 30$	301	1163	
$Ti_{47}Pd_{48}Zr_5$	550	$A_f + 30$	-	628	
$Ti_{47}Pd_{48}Zr_5$	399	$A_s - 30$	302	1449	
$Ti_{48}Pd_{50}Zr_2$	400	$A_s - 30$	631	1504	
$Ti_{48}Pd_{50}Zr_2$	563	$A_f + 30$	-	467	
$Ti_{47}Pd_{50}Zr_3$	563	$A_f + 30$	-	183	
$Ti_{47}Pd_{50}Zr_3$	490	$A_s - 30$	219	666	
$Ti_{47}Pd_{50}Zr_3$	439	$M_f - 30$	234	863	
$Ti_{45}Pd_{50}Zr_5$	538	$A_f + 30$	-	274	[33]
$Ti_{45}Pd_{50}Zr_5$	426	$A_s - 30$	161	722	[33]
$Ti_{45}Pd_{50}Zr_5$	415	$M_f - 30$	298	937	
$Ti_{43}Pd_{50}Zr_7$	536	$A_f + 30$	-	245	
$Ti_{43}Pd_{50}Zr_7$	461	$A_s - 30$	255	733	
$Ti_{43}Pd_{50}Zr_7$	413	$M_f - 30$	227	954	
$Ti_{40}Pd_{50}Zr_{10}$	337	$A_f + 30$	-	386	[33]
$Ti_{40}Pd_{50}Zr_{10}$	225	$A_s - 30$	331	894	[33]
$Ti_{43}Pd_{52}Zr_5$	451	$A_s - 30$	371	1080	
$Ti_{43}Pd_{52}Zr_5$	337	$M_f - 30$	568	1378	
$Ti_{40}Pd_{55}Zr_5$	623	$A_f + 30$	-	386	[35]
$Ti_{40}Pd_{55}Zr_5$	408	$M_f - 30$	1030	1492	[35]
$Ti_{45}Pd_{50}V_5$	591	$A_f + 30$	-	644	[34]
$Ti_{45}Pd_{50}V_5$	413	$M_f - 30$	521	1252	[34]
$Ti_{40}Pd_{55}V_5$	589	$A_f + 30$	643	386	[35]
$Ti_{40}Pd_{55}V_5$	368	$M_f - 30$	744	386	[35]
$Ti_{45}Pd_{50}Nb_5$	625	$A_f + 30$	-	389	[34]
$Ti_{45}Pd_{50}Nb_5$	378	$M_f - 30$	329	836	[34]
$Ti_{40}Pd_{55}Nb_5$	565	$A_f + 30$	601	386	[35]
$Ti_{40}Pd_{55}Nb_5$	330	$M_f - 30$	651	386	[35]
$Ti_{45}Pd_{50}Ta_5$ *	625	$A_f + 30$	-	287	[34]
$Ti_{45}Pd_{50}Ta_5$ *	483	$M_f - 30$	462	941	[34]
$Ti_{45}Pd_{50}Cr_5$	333	$A_f + 30$	-	273	[34]

Table 6. Cont.

Alloy	Test Temp., °C	The Difference from Martensite Transformation Temperature, °C	Detwining Stress, MPa	0.2% Flow Stress, MPa	Ref.
Ti ₄₅ Pd ₅₀ Cr ₅	228	$M_f - 30$	317	1000	[34]
Ti ₄₅ Pd ₅₀ Mo ₅	503	$A_f + 30$	-	364	[34]
Ti ₄₅ Pd ₅₀ Mo ₅	256	$M_f - 30$	512	1239	[34]
Ti ₄₅ Pd ₅₀ W ₅ *	615	$A_f + 30$	-	232	[34]
Ti ₄₅ Pd ₅₀ W ₅ *	474	$M_f - 30$	591	1008	[34]
Ti ₅₀ Pd ₄₈ Ru ₂	320	-	-	301	
Ti ₅₀ Pd ₄₆ Ru ₄	520	$A_f + 30$	-	150	
Ti ₅₀ Pd ₄₆ Ru ₄	320	-	196	598	
Ti ₅₀ Pd ₄₆ Ir ₄	580	$A_f + 30$	-	100	
Ti ₅₀ Pd ₄₆ Ir ₄	454	$M_f - 30$	260	740	
Ti ₅₀ Pd ₄₆ Ir ₄	320	-	280	800	
Ti ₅₀ Pd ₄₂ Ir ₈	551	$A_f + 30$	65	150	
Ti ₅₀ Pd ₄₂ Ir ₈	408	$M_f - 30$	320	720	
Ti ₅₀ Pd ₃₈ Ir ₁₂	521	-	215	744	
Ti ₅₀ Pd ₃₈ Ir ₁₂	401	$M_f - 30$	360	850	
Ti ₅₀ Pd ₄₆ Co ₄	520	$A_f + 30$	-	65	
Ti ₅₀ Pd ₄₆ Co ₄	320	-	200	710	
Ti ₅₀ Pt ₅₀	1100	$A_f + 50$	-	27	[38]
Ti ₅₀ Pt ₅₀	910	$M_f - 50$	-	320	[38]
Ti ₅₀ Pt _{37.5} Ir _{12.5}	1153	$A_f + 50$	-	42	[38]
Ti ₅₀ Pt _{37.5} Ir _{12.5}	928	$M_f - 50$	300	640	[38]
Ti ₅₀ Pt ₂₅ Ir ₂₅	1240	$A_f + 50$	-	35	[38]
Ti ₅₀ Pt ₂₅ Ir ₂₅	1018	$M_f - 50$	230	450	[38]
Ti ₅₀ Pt _{12.5} Ir _{37.5}	1268	$A_f + 50$	-	170	[38]
Ti ₅₀ Pt _{12.5} Ir _{37.5}	1119	$M_f - 50$	285	435	[38]
Ti ₅₀ Pt ₄₅ Ru ₅	-	$A_f + 50$	-	100	[40, 42]
Ti ₅₀ Pt ₄₅ Ru ₅	800	$M_f - 50$	355	712	[42]
Ti ₄₅ Pt ₅₀ Zr ₅	-	$A_f + 50$	-	111	[40, 42]
Ti ₄₅ Pt ₅₀ Zr ₅	790	$M_f - 50$	600	1468	[40, 42]
Ti ₅₀ Pt ₄₅ Co ₅	-	$A_f + 50$	-	72	[40, 43]
Ti ₅₀ Pt ₄₅ Co ₅	-	$M_f - 50$	407	523	[40, 43]
Ti ₄₅ Pt ₅₀ Hf ₅	-	$A_f + 50$	-	149	[40, 44]
Ti ₄₅ Pt ₅₀ Hf ₅	-	$M_f - 50$	565	1113	[40, 44]

*: melting was not perfect.

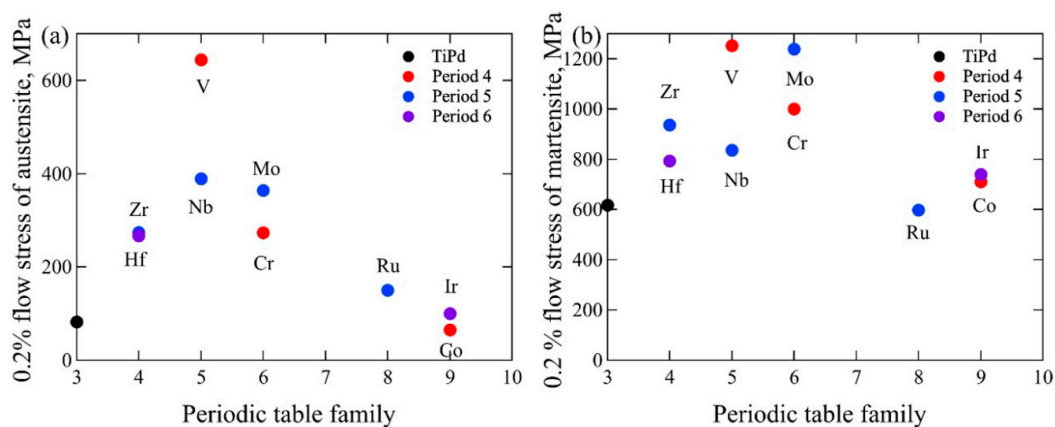


Figure 3. The 0.2% flow stress of the austenite and martensite phases of TiPd [33]: (a) Ti₄₅Pd₅₀X₅ (X = Zr [33], Hf [34], V [34], Nb [34], Cr [34], and Mo [34]) and (b) Ti₅₀Pd₄₆Y₄ (Y = Ru, Co, and Ir) [37] for the periodic table family.

4. Strain Recovery Determined by Thermal Cyclic Test under Constant Stress

Recently, strain recovery was investigated through a thermal cyclic compression test under a constant load (Shimadzu AG-X, Shimadzu, Kyoto, Japan). The specimens were heated to 30 °C above A_f and then cooled to a temperature lower than M_f under a constant load of 15–200 MPa. Five thermal cycles under loads of 15, 50, 100, 150, and 200 MPa were applied for the same samples in the order given with heating and cooling rates of 50 °C/min. The work output (work per volume) was obtained from the product of the recovery strain and the applied stress. The strain temperature (S–T) curves of $Ti_{45}Pd_{50}X_5$ ($X = Zr, Hf, V,$ and Nb) are plotted in Figure 4. The transformation strain increased with an increase in the applied stress. The transformation strains of $Ti_{45}Pd_{50}Zr_5$ and $Ti_{45}Pd_{50}Hf_5$ exceed 2% above 50 MPa, as shown in Figure 4a,b. Nonetheless, the transformation strains of $Ti_{45}Pd_{50}V_5$ are less than 1% at an applied stress of 200 MPa. Phase transformation was not evident in $TiPdNb$, even at 200 MPa. The perfect strain recovery was obtained under a small applied stress of less than 100 MPa in $Ti_{45}Pd_{50}V_5$, but the irrecoverable strain appeared at 150 MPa and increased at 200 MPa. In $Ti_{45}Pd_{50}Zr_5$ and $Ti_{45}Pd_{50}Hf_5$, the small irrecoverable strain was observed, even at 15 MPa, which increased with the applied stress. At 150 and 200 MPa in $Ti_{45}Pd_{50}Hf_5$, trumpet-shaped S–T curves were obtained, as shown by arrows in Figure 4b. This is because the compressive plastic deformation is larger than the expansion of the sample during heating above A_f .

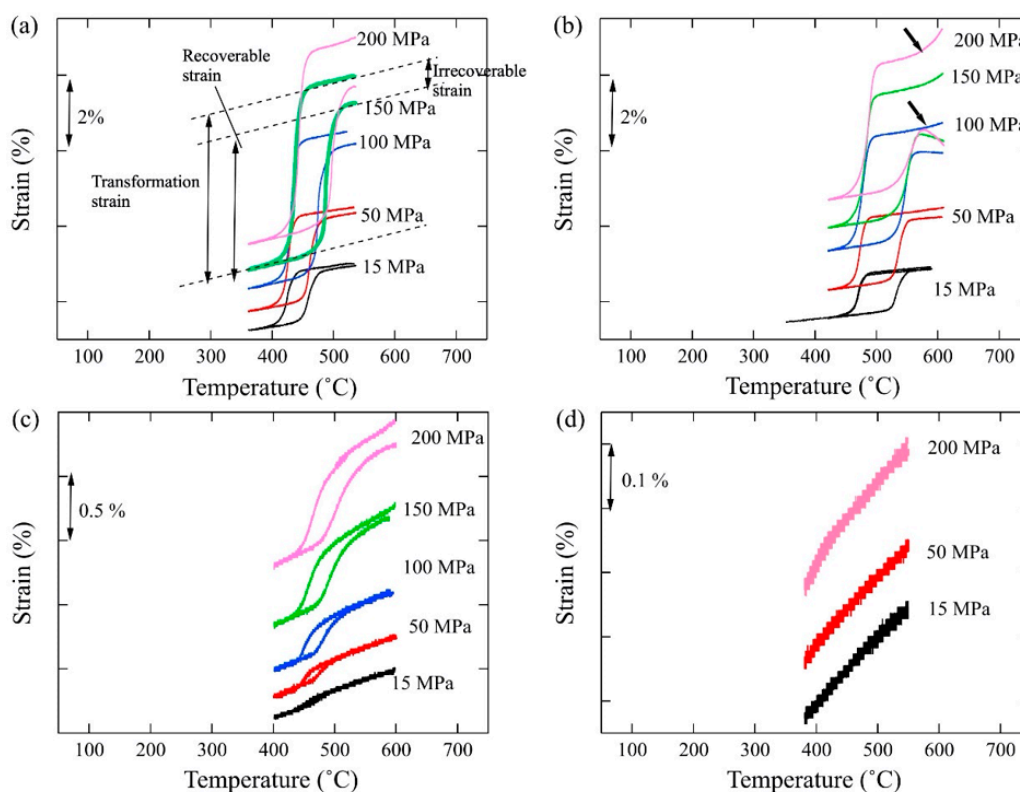


Figure 4. Strain–temperature curves of thermal cycle tests of between 15 and 200 MPa for (a) $Ti_{45}Zr_5Pd_{50}$ [45], (b) $Ti_{45}Hf_5Pd_{50}$, (c) $Ti_{45}V_5Pd_{50}$, and (d) $Ti_{45}Nb_5Pd_{50}$.

The recoverable and irrecoverable strains, as well as the work output of $Ti_{45}Pd_{50}X_5$ ($X = Zr, Hf,$ and V) are plotted as a function of the applied stress, as shown in Figure 5; for reference, those of $Ti_{50}Pd_{50}$ at 50 MPa are also plotted [58]. The recoverable strain increased with the applied stress; however, by increasing the irrecoverable strain, the recoverable strain started to decrease after the peak recoverable strain. Although the recoverable strain of $Ti_{50}Pd_{50}$ is similar to that of $Ti_{45}Pd_{50}X_5$ ($X = Zr$ and Hf), the irrecoverable strain is very large compared to that of the ternary alloys. The irrecoverable strain is expected to increase drastically with an increase in the applied stress. It also indicates that

the addition of an alloying element is effective toward decreasing the irrecoverable strain. The work output increased with applied stress. Although an irrecoverable strain appeared, a large work output of 7.6 J/cm^3 was obtained for $\text{Ti}_{45}\text{Pd}_{50}\text{Zr}_5$.

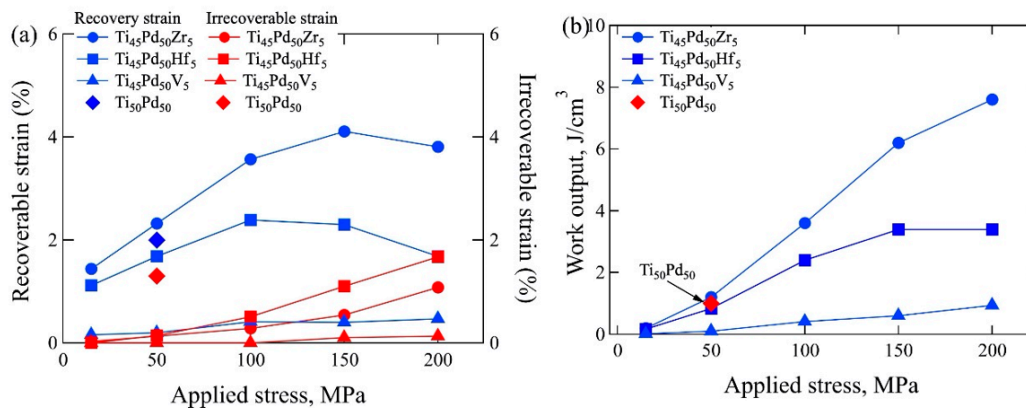


Figure 5. Changes in (a) recoverable strain and irrecoverable strain, and (b) work output for the applied stress of $\text{Ti}_{50}\text{Pd}_{50}$ [58], $\text{Ti}_{45}\text{Pd}_{50}\text{Zr}_5$ [45], $\text{Ti}_{45}\text{Pd}_{50}\text{Hf}_5$, and $\text{Ti}_{45}\text{Pd}_{50}\text{V}_5$ derived from the strain–temperature curves shown in Figure 4.

5. Effects of Training

It is known that repeated thermal cyclic tests, which is referred to as “training,” reduces the irrecoverable strain, and a perfect recovery is finally obtained [8,59]. For example, the irrecoverable strain of TiNi-based alloys became approximately 0 after 40 cycles under a load of 80 MPa. The training was effective for the TiNi alloys strengthened by the addition of Pd or Sc. Therefore, training was performed for $\text{Ti}_{45}\text{Pd}_{50}\text{X}_5$ ($X = \text{Zr}$ and Hf) under a 50-MPa load. The irrecoverable strain vs. the number of thermal cycles is plotted in Figure 6. The irrecoverable strain of $\text{Ti}_{45}\text{Pd}_{50}\text{Zr}_5$ was saturated after 10 cycles, and it remained at approximately 0.1%. The irrecoverable strain of $\text{Ti}_{45}\text{Pd}_{50}\text{Hf}_5$ was approximately double that of $\text{Ti}_{45}\text{Pd}_{50}\text{Zr}_5$, and it was unsaturated. This indicates that the strain recovery of ternary alloys is unstable for repeated cycles. The effect of Zr content on the training effect was investigated for $\text{Ti}_{45}\text{Pd}_{50}\text{Zr}_7$ and $\text{Ti}_{45}\text{Pd}_{50}\text{Zr}_{10}$ [36]. By increasing Zr addition, the irrecoverable strain finally disappeared during training and perfect strain recovery was achieved [36]. This outcome can be attributed to two reasons: (1) the solid-solution hardening effect is larger at high Zr contents, and (2) MTT reduction advantageously affects the suppression of plastic deformation.

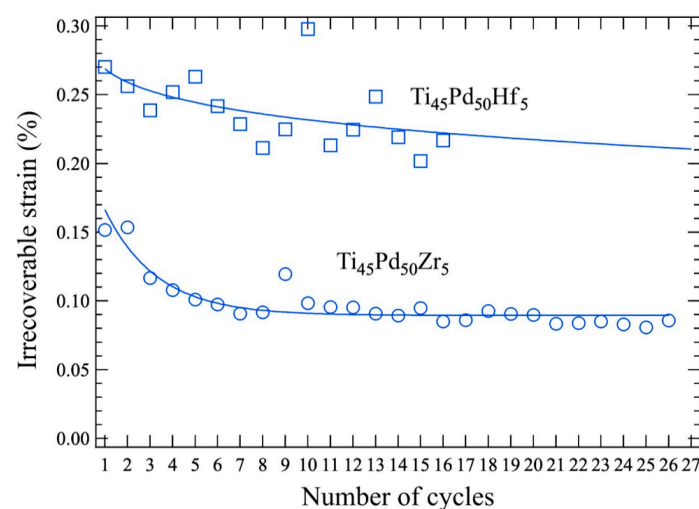


Figure 6. Irrecoverable strain of $\text{Ti}_{45}\text{Pd}_{50}\text{Zr}_5$ and $\text{Ti}_{45}\text{Pd}_{50}\text{Hf}_5$ as a function of number of thermal cycles under 50 MPa.

6. Strain Recovery of Multi-Component Alloys

A thermal cyclic test was performed on the multi-component alloys to investigate strain recovery. Some results have already been published [45–50]. The recoverable and irrecoverable strains, as well as the work output of some of the multi-component alloys are shown in Figure 7; the TiZrPdNi and TiZrPdPt alloys are shown in Figure 7a,c,e, and in Figure 7b,d,f, respectively, while Ti₄₅Pd₅₀Zr₅ is shown as a standard sample in all the diagrams. Furthermore, Ti₄₅Zr₅Pd₄₅Ni₅, Ti₄₅Zr₅Pd₃₇Ni₁₃, Ti₄₀Zr₁₀Pd₂₅Pt₂₅, and Ti₄₅Zr₅Pd₂₅Pt₂₀Ni₅ are the original data source in this study. In Figure 7a,c,e, the concentrations of Ti and Zr were maintained at 45 and 5 at%, respectively, in TiZrPdNi, and only the concentrations of Pd and Ni were changed. Among the tested alloys in Figure 7a,c,e, TiZrPdNi alloys exhibited a relatively high recoverable strain, although the recoverable strain of Ti₄₅Zr₅Pd₄₀Ni₁₀ [48] was similar to that of ternary Ti₄₅Pd₅₀Zr₅. Moreover, Ni addition seems to increase the recoverable strain of Ti₄₅Pd₅₀Zr₅. The recoverable strain of Ti₄₅Zr₅Pd₄₀Co₁₀ [48] was very small, thereby suggesting that Co addition drastically decreased the recovery strain. However, the recoverable strain of the multi-component alloys of TiZrPdNiCo was larger than that of Ti₄₅Zr₅Pd₄₀Ni₁₀ [48]. This indicated that the recoverable strain was increased by the effect of the multi-component alloy, i.e., the high-entropy effect. In Figure 7c, the irrecoverable strains of most of the tested alloys were smaller than 0.2%. Only the ternary Ti₄₅Pd₅₀Zr₅ and quaternary alloy of Ti₄₅Zr₅Pd₄₅Ni₅, which were defined as LEA, represented a large irrecoverable strain exceeding 0.2%. A decrease in the irrecoverable strain of MEAs is also considered to be consequent of the high-entropy effect. As a result of the large recoverable strain, the work output of TiZrPdNi-type multi-component alloys also becomes large, as shown in Figure 7e. The work outputs of some alloys exceeded 10 J/cm³. The repeated thermal cycling test, i.e., training was also applied for some alloys. For example, training under 300 MPa was performed for Ti₄₅Zr₅Pd₄₀Ni₁₀ for 100 cycles [48]. Although the transformation strain decreased, the irrecoverable strain decreased, and a perfect recovery was finally achieved during the thermal cyclic test. The final recovery strain was approximately 3.6% under 300 MPa. Thereafter, the work output was 10.8 J/cm³ at the A_f of 258 °C. For Ti₄₅Zr₅Pd₄₀Co₁₀, training was performed under 700 MPa. After nine cycles, the irrecoverable strain disappeared, and a perfect recovery was achieved. The final recovery strain was approximately 1%, and the work output was 7 J/cm³ at the A_f of 361 °C.

In Figure 7b,d,f, TiZrPdPt alloys are compared. Again, the concentrations of Ti and Zr were maintained at 45 and 5 at%, respectively, in most of the alloys. Compared with the recoverable strain in TiZrPdNi alloys, as shown in Figure 7a and in TiZrPdPt alloys, as presented in Figure 7b, those of TiZrPdPt alloys were smaller than 3% and less than those of TiZrPdNi alloys. This indicates that the addition of Pt decreases the recoverable strain. The same trend can be observed in quaternary alloys by comparing Ti₄₅Zr₅Pd₂₅Pt₂₅ and Ti₄₅Zr₅Pd₄₅Pt₅. A small recoverable strain was achieved in the alloy with high Pt content. The effect of Zr on the recoverable strain in quaternary alloys could be understood by comparing Ti₄₀Zr₁₀Pd₂₅Pt₂₅ and Ti₄₅Zr₅Pd₂₅Pt₂₅, and it was found that Zr addition increased the recoverable strain. In the multi-component alloys, it was found that high Pt addition decreased recoverable strain, as shown in Figure 7b. In TiZrPdPt alloys, it was found that the irrecoverable strain decreased in the multi-component alloys including the MEAs and HEAs, except for the LEA, Ti₄₅Zr₅Pd₄₅Pt₅, as shown in Figure 7d. The irrecoverable strain of Ti₄₅Zr₅Pd₂₅Pt₂₅ is also small, which may be due to high MTT. The work outputs of the TiZrPdPt alloys are shown in Figure 7f; they are all between 2–6 J/cm³ and smaller than that of Ti₄₅Pd₅₀Zr₅.

Training was performed for Ti₄₅Zr₅Pd₂₀Pt₂₅Ni₅ and Ti₄₅Zr₅Pd₂₀Pt₂₀Ni₁₀ [49], and perfect recovery was achieved during the thermal cyclic test for approximately 100 cycles under loads of 200, 300, and 400 MPa, whereby the final work outputs were approximately 3.5, 3, and 2 J/cm³, respectively, for Ti₄₅Zr₅Pd₂₀Pt₂₅Ni₅. For Ti₄₅Zr₅Pd₂₀Pt₂₀Ni₁₀, final work outputs of 3 and 1.5 J/cm³ under loads of 200 and 300 MPa were obtained, respectively. The small work output for the large applied stress represents a drastic decrease in the transformation strain. It is necessary to keep the transformation strain of the multi-component alloys during the thermal cyclic test. The thermal cyclic test is considered

as a kind of thermal fatigue test and the stable cyclic strain recovery with the constant transformation strain indicates the thermal fatigue life of SMAs and stability as SMA actuators.

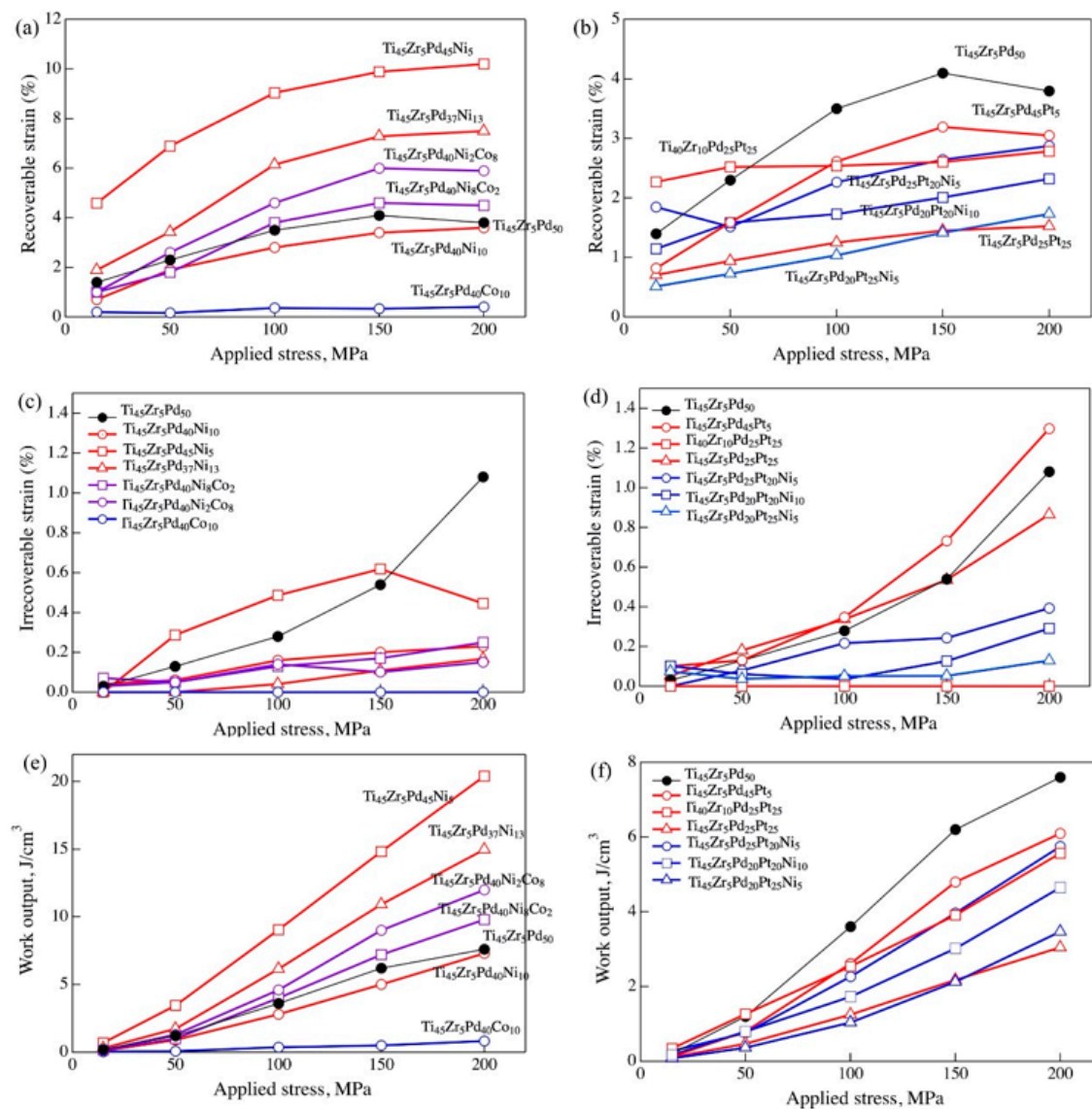


Figure 7. (a,b) Recoverable strain, (c,d) irrecoverable strain, and (e,f) work output obtained from strain–temperature curves of thermal cycle tests of between 15 and 200 MPa for $\text{Ti}_{45}\text{Zr}_5\text{Pd}_{50}$ [45] and multi-component alloys. (a,c,d) TiZrPdNi alloys [47,48], and (b,d,f) TiZrPdPt alloys [45,47,49].

The strength of the austenite and martensite phases of some of the multi-component alloys are investigated, and the results are summarized in Table 7. The strength of the austenite phases in the tested alloys was between 200 and 300 MPa, and they were similar to those of the ternary alloys. This is because the MTTs of the multi-component alloys are relatively high. Therefore, it is difficult to correlate the strength and strain recovery directly. Thereafter, the temperature dependence of the strength of the martensite and austenite phases was investigated for ternary and multi-component alloys [49]. The strength of the multi-component alloys was higher in both martensite and austenite phases when compared at the same temperature. The solid-solution strengthening effect of the multi-component alloys was more evident when the strength of the austenite phase was compared at the same test temperature of 700 °C. The strength of the multi-component alloys was higher than that of the ternary alloys or LEAs.

Table 7. Strength of the martensite and austenite phases of the multi-element alloys.

Alloy	Test Temp., °C	The Difference from Martensite Transformation Temperature, °C	Detwining Stress, MPa	0.2% Flow Stress, MPa	Ref.
Ti ₄₅ Pd ₄₅ Pt ₅ Zr ₅	-	A _f + 30	-	281	[45]
Ti ₄₅ Pd ₄₅ Pt ₅ Zr ₅	425	M _f - 30	246	877	[45]
Ti ₄₅ Pd ₃₅ Pt ₁₅ Zr ₅	-	A _f + 30	-	315	[45]
Ti ₄₅ Pd ₃₅ Pt ₁₅ Zr ₅	442	M _f - 30	387	1080	[45]
Ti ₄₅ Pd ₂₅ Pt ₂₅ Zr ₅	-	A _f + 30	-	231	[45]
Ti ₄₅ Pd ₂₅ Pt ₂₅ Zr ₅	509	M _f - 30	436	1205	[45]
Ti ₄₅ Zr ₅ Pd ₂₀ Ni ₅ Pt ₂₅	628	A _f + 30	-	322	[49]
Ti ₄₅ Zr ₅ Pd ₂₀ Ni ₅ Pt ₂₅	402	M _f - 30	-	1266	[49]
Ti ₄₅ Zr ₅ Pd ₂₀ Ni ₁₀ Pt ₂₀	472	A _f + 30	-	610	[49]
Ti ₄₅ Zr ₅ Pd ₂₀ Ni ₁₀ Pt ₂₀	226	M _f - 30	-	1615	[49]
Ti ₄₅ Zr ₅ Pd ₂₅ Pt ₂₀ Au ₅	620	A _f + 30	-	267	[50]
Ti ₄₅ Zr ₅ Pd ₂₅ Pt ₂₀ Au ₅	423	M _f - 30	-	1169	[50]
Ti ₄₅ Zr ₅ Pd ₂₅ Pt ₂₀ Co ₅	568	A _f + 30	-	269	[50]
Ti ₄₅ Zr ₅ Pd ₂₅ Pt ₂₀ Co ₅	294	M _f - 30	-	741	[50]

7. Change in Microstructure before and after Training

The microstructural changes during training were also investigated in Ti₄₃Zr₇Pd₅₀ and Ti₄₀Zr₁₀Pd₅₀ [36], Ti₄₅Zr₅Pd₃₅Pt₁₅ [45], as well as Ti₅₀Pd₅₀ [58]. A typical twin structure with multiple variants was observed in the heat-treated sample, but variant selection occurred during the thermal cyclic test, and the major variant was predominantly the [010] axis parallel to the compression axis in all observed alloys. It is suggested that a martensite variant is selected to obtain the largest constriction of the lattice during the compression test. The crystal orientation relationship between the B2 and B19 structures is shown as follows:

$$[110]_{B2} // [100]_{B19}, [010]_{B2} // [010]_{B19}, [\bar{1}10]_{B2} // [001]_{B19}$$

The lattice parameters of the orthorhombic B19 structure of TiPd were $a = 0.459$, $b = 0.28$, and $c = 0.484$ nm [60]. The lattice parameter of b in the B19 structure was the smallest, and the reorientation of the martensite variant along the [010] direction is, therefore, considered to relax the compressive strain under compressive stress.

8. Potential of High-Temperature Shape Memory Alloys (HT-SMAs)

The work outputs obtained by the thermal cyclic test are plotted for A_f , as shown in Figure 8. The open symbols indicate the alloys with imperfect recovery after a single thermal cycle, while solid symbols indicate perfect recovery after training. The green square indicates the work output of Ni_{50.3}Ti_{29.7}Hf₂₀ with nano-sized precipitation, which is developed in the USA and is the most expected HT-SMA [16,19]. It is said that the work output of the commercially used TiNi is between 12–18 J/cm³ for operating temperatures under 100 °C [61]. The work output of Ni_{50.3}Ti_{29.7}Hf₂₀ is equivalent to that of TiNi alloys at higher A_f (220 °C) than TiNi. Although the work outputs of some alloys in my group's research exceed 12 J/cm³ at approximately 200 °C [48], most of them underwent decreasing work outputs with increasing A_f . Nevertheless, it is notable that perfect recovery is achieved at temperatures between 200–600 °C because it is difficult to obtain above 200 °C. The work output obtained at 600 °C was approximately 3 J/cm³.

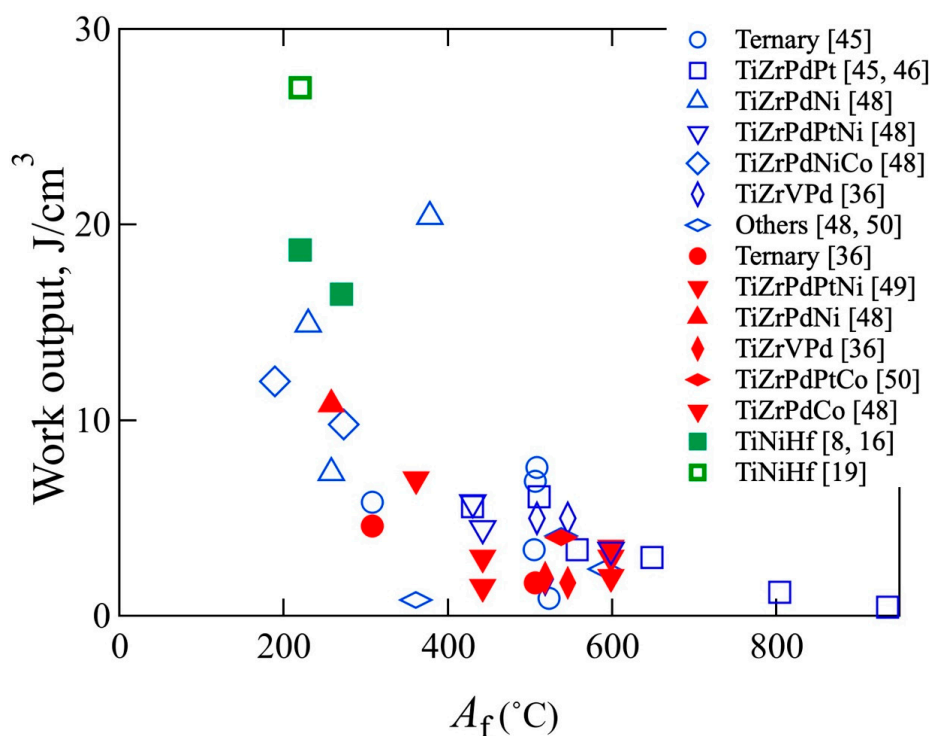


Figure 8. Work output vs. A_f . The open and solid symbols represent the work output of the alloys with imperfect recovery and the work output of the alloys with perfect recovery.

9. Conclusions

This paper reviewed TiPd- and TiPt-based HT-SMAs. The effects of alloying elements on phase transformation, strain recovery, and strength are shown in ternary TiPd and TiPt alloys. In most cases, MTT decreased through the addition of alloying elements, as well as an increase in the alloying element content. The alloying element improved the strength of the martensite and austenite phases by the solid-solution strengthening effect. However, it is difficult to correlate with solid-solution strengthening and strain recovery. A thermal cyclic test was performed to investigate the strain recovery. The irrecoverable strain decreased with the addition of an alloying element, but it was difficult to achieve perfect recovery, even after repeated thermal cyclic tests (training). Multi-component alloys were also investigated. Notably, MTT can be controlled by a combination of the constituent elements. For example, Zr, Ni, and Co decreased MTT, whereas Pt increased MTT. The effect of alloying elements on the recoverable strain differed from that of the MTT. For example, Ni increased the recoverable strain, while Pt and Co decreased it. The extra solid-solution hardening effect relative to ternary alloys was found in the multi-component alloys. Consequently, the irrecoverable strains were smaller in the multi-component alloys than those in the ternary alloys. In many cases, training was effective in achieving perfect recovery in the multi-component alloys; however, a decrease in the transformation strain also occurred. Multi-component alloys can be good candidates for HT-SMAs; the limitations that need to be overcome entail the suppression of the transformation strain reduction and temperature hysteresis increment.

Funding: The study was partly supported by “Precious Metals Research Grant of TANAKA Memorial Foundation”, for which the author expresses her thanks.

Acknowledgments: This work was performed in cooperation with M. Kawakita, A. Wadood, and R. Arockiakumar as a part of their Post-doctoral research; W. Tasaki and W. Takebe as a part of their Bachelors research; H. Sato and H. Matsuda as a part of their Bachelors and Masters research; and B. Ohl, K. Bogdanowicz, E. Muszalska, D. Kuczyska, A. Wierzchowska, A. Chmielewska, K. Aimizu, and M. Yamamoto as a part of their internship program.

Conflicts of Interest: The author declares no conflict of interest.

References

1. DeCastro, J.A.; Melcher, K.J.; Noebe, R.D. NASA/TM-2005-213834, AIAA-2005-3988. Available online: <https://ntrs.nasa.gov/citations/20050203852> (accessed on 30 September 2020).
2. Stebner, A.; Padula, S., II; Noebe, R.; Lerch, B.; Quinn, D. Development, Characterization, and Design Considerations of Ni_{19.5}Ti_{50.5}Pd₂₅Pt₅ High-temperature Shape Memory Alloy Helical Actuators. *J. Intell. Mater. Syst. Struct.* **2009**, *20*, 2107–2126. [[CrossRef](#)]
3. Benefan, O.; Brown, J.; Calkins, F.T.; Kumar, P.; Stebner, A.P.; Turner, T.L.; Vaidyanathan, R.; Webster, J.; Young, M.L. Shape memory alloy actuator design: CASMART collaborative best practices and case studies. *Int. J. Mech. Mater. Des.* **2014**, *10*, 1–42. [[CrossRef](#)]
4. Ma, J.; Karaman, I.; Noebe, R.D. High temperature shape memory alloys. *Int. Mater. Rev.* **2010**, *55*, 257–315. [[CrossRef](#)]
5. Bigelow, G.S.; Padula, S.A., II; Garg, A.; Gaydosh, D.; Noebe, R.D. Characterization of ternary NiTiPd high-temperature shape-memory alloys under load-biased thermal cycling. *Metall. Mater. Trans. A* **2010**, *41*, 3065–3079. [[CrossRef](#)]
6. “Development of a Numerical Model for High-Temperature Shape Memory Alloys” NASA Technical Reports Server, 2013. Available online: <https://ntrs.nasa.gov/citations/20060028493> (accessed on 30 September 2020).
7. Atli, K.C.; Karaman, I.; Noebe, R.D.; Garg, A.; Chumlyakov, Y.I.; Kireeva, I.V. Improvement in the Shape Memory Response of Ti_{50.5}Ni_{24.5}Pd₂₅ High-Temperature Shape Memory Alloy with Scandium Microalloying. *Metall. Mater. Trans. A* **2010**, *41*, 2485–2497. [[CrossRef](#)]
8. Atli, K.C.; Karaman, I.; Noebe, R.D.; Maier, H.J. Comparative analysis of the effects of severe plastic deformation and thermomechanical training on the functional stability of Ti_{50.5}Ni_{24.5}Pd₂₅ high-temperature shape memory alloy. *Scr. Mater.* **2011**, *64*, 315–318. [[CrossRef](#)]
9. Atli, K.C.; Karaman, I.; Noebe, R.D. Work output of the two-way shape memory effect in Ti_{50.5}Ni_{24.5}Pd₂₅ high-temperature shape memory alloy. *Scr. Mater.* **2011**, *65*, 903–906. [[CrossRef](#)]
10. Atli, K.C.; Karaman, I.; Noebe, R.D.; Garg, A.; Chumlyakov, Y.I.; Kireeva, I.V. Shape memory characteristics of Ti_{50.5}Ni_{24.5}Pd₂₅Sc_{0.5} high-temperature shape memory alloy after severe plastic deformation. *Acta Mater.* **2011**, *59*, 4747–4760. [[CrossRef](#)]
11. Yang, F.; Coughlin, D.R.; Phillips, P.J.; Yang, L.; Devaraj, A.; Kovarik, L. Structure analysis of a precipitate phase in an Ni-rich high-temperature NiTiHf shape memory alloy. *Acta Mater.* **2013**, *61*, 3335–3346. [[CrossRef](#)]
12. Santamarta, R.; Arroyave, R.R.; Pons, J.; Evrigen, A.; Karaman, I.; Karacka, H.E.; Noebe, R.D. TEM study of structural and microstructural characteristics of a precipitate phase in Ni-rich Ni-Ti-Hf and Ni-Ti-Zr shape memory alloys. *Acta Mater.* **2013**, *61*, 6191–6206. [[CrossRef](#)]
13. Bigelow, G.S.; Garg, A.; Padula, S.A., II; Gaydosh, D.J.; Noebe, R.D. Load-biased shape-memory and superelastic properties of a precipitation strengthened high-temperature Ni_{50.3}Ti_{29.7}Hf₂₀ alloy. *Scr. Mater.* **2011**, *64*, 725–728. [[CrossRef](#)]
14. Coughlin, D.R.; Phillips, P.J.; Bigelow, G.S.; Garg, A.; Noebe, R.D.; Mills, M.J. Characterization of the microstructure and mechanical properties of a 50.3Ni-29.7Ti-20Hf shape memory alloy. *Scr. Mater.* **2012**, *67*, 112–115. [[CrossRef](#)]
15. Evrigen, A.; Basner, F.; Karaman, I.; Noebe, R.D.; Pons, J.; Santamarta, R. Effect of Aging on the martensitic transformation characteristics of a Ni-rich NiTiHf high temperature shape memory alloys. *Funct. Mater. Lett.* **2012**, *5*, 1250038. [[CrossRef](#)]
16. Karaca, H.E.; Saghaian, S.M.; Ded, G.; Tobe, H.; Basaran, B.; Maier, H.J.; Noebe, R.D.; Chumlyakov, Y.I. Effects of nanoprecipitation on the shape memory and material properties of an Ni-rich NiTiHf high temperature shape memory alloy. *Acta Mater.* **2013**, *61*, 7422–7431. [[CrossRef](#)]
17. Benafan, O.; Garg, A.; Noebe, R.D.; Bigelow, G.S.; Padula, S.A.; Gaydosh, D.J.; Schell, N.; Mabe, J.H.; Vaidyanathan, R. Mechanical and functional behavior of Ni-rich Ni_{50.3}Ti_{29.7}Hf₂₀ high temperature shape memory alloy. *Intermet* **2014**, *50*, 94–107. [[CrossRef](#)]
18. Evrigen, A.; Karaman, I.; Santamarta, R.; Pons, J.; Hayrettin, C.; Noebe, R.D. Relationship between crystallographic compatibility and thermal hysteresis in Ni-rich NiTiHf and NiTiZr high temperature shape memory alloys. *Acta Mater.* **2016**, *121*, 374–383. [[CrossRef](#)]

19. Saghaian, S.M.; Karaca, H.E.; Tobe, H.; Turabi, A.S.; Saedi, S.; Saghaian, S.E.; Chumlyakov, Y.I.; Noebe, R.D. High strength NiTiHf shape memory alloys with tailorable properties. *Acta Mater.* **2017**, *134*, 211–220. [[CrossRef](#)]
20. Amin-Ahmadi, B.; Gallmeyer, T.; Pauza, J.G.; Duerig, T.W.; Noebe, R.D.; Stebner, A.P. Effect of a pre-aging treatment on the mechanical behaviors of Ni_{50.3}Ti_{49.7-x}Hf_x (x < 9 at.%) Shape memory alloys. *Scr. Mater.* **2018**, *147*, 11–15.
21. Amin-Ahmadi, B.; Pauza, J.G.; Shamimi, A.; Duerig, T.W.; Noebe, R.D.; Stebner, A.P. Coherency strains of H-phase precipitates and their influence on functional properties of nickel-titanium-hafnium shape memory alloys. *Scr. Mater.* **2018**, *147*, 83–87. [[CrossRef](#)]
22. Evirgen, A.; Pons, J.; Karaman, I.; Santamarta, R.; Noebe, R.D. H-Phase Precipitation and Martensitic Transformation in Ni-rich Ni-Ti-Hf and Ni-Ti-Zr High-Temperature Shape Memory Alloys. *Shap. Mem. Superelasticity* **2018**, *4*, 85–92. [[CrossRef](#)]
23. Amin-Ahmadi, B.; Noebe, R.D.; Stebner, A.P. Crack propagation mechanisms of an aged nickel-titanium-hafnium shape memory alloy. *Scr. Mater.* **2019**, *159*, 85–88. [[CrossRef](#)]
24. Karakoc, O.; Atli, K.C.; Evirgen, A.; Pons, J.; Santamarta, R.; Benafan, O.; Noebe, R.D.; Karaman, I. Effects of training on the thermomechanical behavior of NiTiHf and NiTiZr high temperature shape memory alloys. *Mater. Sci. Eng. A* **2020**, *794*, 139857. [[CrossRef](#)]
25. ASM Alloy Phase Diagrams Center; Villars, P.; Okamoto, H.; Cenzual, K. (Eds.) ASM International, Materials Park, OH, 2006. Available online: <http://www1.asminternational.org/AsmEnterprise/APD> (accessed on 4 September 2020).
26. Donkersloot, H.C.; van Vocht, J.H.N. Martensitic transformations in gold-titanium, palladium-titanium and platinum-titanium alloys near the equiatomic composition. *J. Less Common Met.* **1970**, *20*, 83–91. [[CrossRef](#)]
27. Biggs, T.; Witcomb, M.J.; Cornish, L.A. Martensite-type transformations in platinum alloys. *Mater. Sci. Eng. A* **1999**, *273–278*, 204–207. [[CrossRef](#)]
28. Biggs, T.; Corite, M.B.; Witcomb, M.J.; Cornish, L.A. Martensitic Transformations, Microstructure, and Mechanical Workability of TiPt. *Metall. Trans. A* **2003**, *32A*, 2267–2272. [[CrossRef](#)]
29. Otsuka, K.; Oda, K.; Ueno, Y.; Piao, M.; Ueki, T.; Horikawa, H. The shape memory effect in a Ti₅₀Pd₅₀ alloy. *Scr. Met. Mater.* **1993**, *29*, 1355–1358. [[CrossRef](#)]
30. Declairieux, C.; Denquin, A.; Ochin, P.; Poriter, R.; Vermaut, P. On the potential of Ti₅₀Au₅₀ compound as a high temperature shape memory alloy. *Intermetallics* **2011**, *19*, 1461–1465. [[CrossRef](#)]
31. Wadood, A.; Hosoda, H.; Yamabe-Mitarai, Y. Phase transformation, oxidation and shape memory properties of Ti-50Au-10Zr alloy for high temperature applications. *J. Alloys Compd.* **2014**, *595*, 200–205. [[CrossRef](#)]
32. Wadood, A.; Yamabe-Mitarai, Y. Silver- and Zirconium-added ternary and quaternary TiAu based high temperature shape memory alloys. *J. Alloys Compd.* **2015**, *646*, 1172–1177. [[CrossRef](#)]
33. Kawakita, M.; Takahashi, M.; Takahashi, S.; Yamabe-Mitarai, Y. Effect of Zr on phase transformation and high-temperature shape memory effect in TiPd alloys. *Mater. Lett.* **2012**, *89*, 336–338. [[CrossRef](#)]
34. Yamabe-Mitarai, Y. Development of High-Temperature Shape Memory Alloys above 673 K. *Mater. Sci. Forum* **2017**, *879*, 107–112. [[CrossRef](#)]
35. Arockiakumar, R.; Takahashi, M.; Takahashi, S.; Yamabe-Mitarai, Y. Microstructure, mechanical and shape memory properties of Ti-55Pd-5x (x = Zr, Hf, V, Nb) alloys. *Mater. Sci. Eng. A* **2013**, *585*, 86–93. [[CrossRef](#)]
36. Sato, H.; Kim, H.Y.; Shimojo, M.; Yamabe-Mitarai, Y. Training effect on microstructure and shape recovery in Ti-Pd-Zr alloys. *Mater. Trans.* **2017**, *10*, 1479–1486. [[CrossRef](#)]
37. Yamabe-Mitarai, Y.; Wadood, A.; Arockiakumar, R.; Hara, T.; Takahashi, M.; Takahashi, S.; Hosoda, H. High-Temperature Shape Memory Alloys Based on Ti-Platinum Group Metals compounds. *Mater. Sci. Forum* **2014**, *783–786*, 2541–2545. [[CrossRef](#)]
38. Yamabe-Mitarai, Y.; Hara, T.; Miura, S.; Hosoda, H. Mechanical properties of Ti-50(Pt, Ir) high-temperature shape memory alloys. *Mater. Trans.* **2006**, *47*, 650–657. [[CrossRef](#)]
39. Yamabe-Mitarai, Y.; Hara, T.; Miura, S.; Hosoda, H. Phase transformation and shape memory effect of Ti(Pt, Ir). *Metall. Trans. A* **2012**, *43A*, 2901–2911. [[CrossRef](#)]
40. Yamabe-Mitarai, Y.; Arockiakumar, R.; Wadood, A.; Suresh, K.S.; Kitashima, T.; Hara, T.; Shimojo, M.; Tasaki, W.; Takahashi, M.; Takahashi, S.; et al. Ti(Pt, Pd, Au) based high temperature shape memory alloys. *Mater. Today* **2015**, *2S*, S517–S522. [[CrossRef](#)]

41. Yamabe-Mitarai, Y.; Hara, T.; Kitashima, T.; Miura, S.; Hosoda, H. Composition dependence of phase transformation behavior and shape memory effect of Ti(Pt, Ir). *J. Alloys Compd.* **2013**, *577S*, S399–S403. [[CrossRef](#)]
42. Wadood, A.; Takahashi, M.; Takahashi, S.; Hosoda, H.; Yamabe-Mitarai, Y. High-temperature mechanical and shape memory properties of TiPt-Zr and TiPt-Ru alloys. *Mater. Sci. Eng. A* **2013**, *564*, 34–41. [[CrossRef](#)]
43. Wadood, A.; Yamabe-Mitarai, Y. TiPt-Co and TiPt-Ru high temperature shape memory alloys. *Mater. Sci. Eng. A* **2014**, *610*, 106–110. [[CrossRef](#)]
44. Wadood, A.; Yamabe-Mitarai, Y. Recent research and developments related to near-equiatomic titanium-platinum alloys for high-temperature applications. *Platinum Metals Rev.* **2014**, *2*, 61–67. [[CrossRef](#)]
45. Tasaki, W.; Shimojo, M.; Yamabe-Mitarai, Y. Thermal cyclic properties of Ti-Pd-Pt-Zr high-temperature shape memory alloys. *Crystals* **2019**, *9*, 595. [[CrossRef](#)]
46. Yamabe-Mitarai, Y.; Takebe, W.; Shimojo, M. Phase transformation and shape memory effect of Ti-Pd-Pt-Zr high-temperature shape memory alloys. *Shap. Mem. Superelasticity* **2017**, *3*, 381–391. [[CrossRef](#)]
47. Yamabe-Mitarai, Y.; Tasaki, W.; Ohl, B.; Sato, H. Effect of Ni, Co, and Pt on Phase transformation and shape recovery of TiPd high temperature shape memory alloys. In Proceedings of the International Conference on Processing & Manufacturing of Advanced Materials, Paris, France, 9–13 July 2018.
48. Yamabe-Mitarai, Y.; Ohl, B.; Bogdanowicz, K.; Muszalska, E. Effect of Ni and Co on Phase Transformation and Shape Memory Effect of Ti-Pd-Zr alloys. *Shap. Mem. Superelasticity* **2020**, *6*, 170–180. [[CrossRef](#)]
49. Matsuda, H.; Sato, H.; Shimojo, M.; Yamabe-Mitarai, Y. Improvement of high-temperature shape-memory effect by multi-component alloy for TiPd alloys. *Mater. Trans.* **2019**, *11*, 2282–2291. [[CrossRef](#)]
50. Matsuda, H.; Shimojo, M.; Murakami, H.; Yamabe-Mitarai, Y. Martensitic Transformation of High-Entropy and Medium-Entropy Shape Memory Alloys. *Mater. Sci. Forum* **2021**, *1016*, 1802–1810.
51. Yeh, J.W.; Chen, S.K.; Lin, S.J.; Gan, J.Y.; Chin, T.S.; Shun, T.T.; Tsau, C.H.; Chang, S.Y. Nanostructured high-entropy alloys with multiple principal elements: Novel alloy design concepts and outcomes. *Adv. Eng. Mater.* **2004**, *6*, 299–303. [[CrossRef](#)]
52. Canter, B.; Chang, I.T.H.; Knight, P.; Vincent, A.J.B. Microstructural development in equiatomic multicomponent alloys. *Mater. Sci. Eng. A* **2004**, *375–377*, 213–218. [[CrossRef](#)]
53. Firstov, G.S.; Kosorukova, T.A.; Koval, Y.N.; Odnosum, V.V. High entropy shape memory alloys. *Mater. Today* **2015**, *2S*, S499–S504. [[CrossRef](#)]
54. Chen, C.-H.; Chen, Y.-J. Shape memory characteristics of (TiZrHf)₅₀Ni₂₅Co₁₀Cu₁₅ high entropy shape memory alloy. *Scr. Mater.* **2019**, *162*, 185–189. [[CrossRef](#)]
55. Canadinc, D.; Trehern, W.; Ma, J.; Karaman, I.; Sun, F.; Chaudhry, Z. Ultra-high temperature multi-component shape memory alloys. *Scr. Mater.* **2019**, *158*, 83–87. [[CrossRef](#)]
56. Yamabe-Mitarai, Y.; Hara, T.; Phasha, M.; Ngoepe, P.; Chikwanda, H. Phase transformation and crystal structure of IrTi. *Intermetallics* **2012**, *31*, 26–33. [[CrossRef](#)]
57. Available online: [https://en.wikipedia.org/wiki/Atomic_radii_of_the_elements_\(data_page\)](https://en.wikipedia.org/wiki/Atomic_radii_of_the_elements_(data_page)) (accessed on 1 September 2020).
58. Hisada, S.; Matsuda, M.; Yamabe-Mitarai, Y. Shape Change and Crystal Orientation of B19 Martensite in Equiatomic TiPd Alloy by Isobaric Test. *Metals* **2020**, *10*, 375. [[CrossRef](#)]
59. Atli, K.C.; Franco, E.B.; Karaman, I.; Gaydos, D.; Noebe, R.D. Influence of crystallographic compatibility on residual strain of TiNi based shape memory alloys during thermo-mechanical cycling. *Mater. Sci. Eng. A* **2013**, *574*, 9–16. [[CrossRef](#)]
60. *Pearson's Crystal Data—Crystal Structure Database for Inorganic Compounds (on CD-ROM)*; Villars, P.; Cenzual, K. (Eds.) ASM International: Materials Park, OH, USA, 2010.
61. Karaca, H.E.; Acar, E.; Tobe, H.; Saghaian, S.M. NiTiHf-based shape memory alloys. *Mater. Sci. Technol.* **2014**, *30*, 1530–1544. [[CrossRef](#)]

Publisher's Note: MDPI stays neutral with regard to jurisdictional claims in published maps and institutional affiliations.



© 2020 by the author. Licensee MDPI, Basel, Switzerland. This article is an open access article distributed under the terms and conditions of the Creative Commons Attribution (CC BY) license (<http://creativecommons.org/licenses/by/4.0/>).